Geophysical Journal International

*Geophys. J. Int.* (2022) **230,** 643–653
Advance Access publication 2022 February 25
GJI Marine Geosciences and Applied Geophysics

https://doi.org/10.1093/gji/ggac077

# Accelerated 2.5-D inversion of airborne transient electromagnetic data using reduced 3-D meshing

Kim Wann Engebretsen,[1] Bo Zhang,[1,2] Gianluca Fiandaca,[1,3] Line Meldgaard Madsen,[1,4] Esben Auken[1,5] and Anders Vest Christiansen[1,4]

[1] *Department of Geoscience, Aarhus University, C. F. Møllers Alle* 4, 8000 *Aarhus C, Denmark. E-mail:* linemeldgaard@geo.au.dk
[2] *Institute of Earth Exploration Science and Technology, Jilin University,* 130026 *Changchun, Jilin, China*
[3] *Department of Earth Sciences, Università degli Studi di Milano,* 20122 *Milano MI, Italy*
[4] *Aarhus University Centre for Water Technology (WATEC), Aarhus University,* 8000 *Aarhus C, Denmark*
[5] *Geological Survey of Denmark and Greenland,* 1350 *Copenhagen, Denmark*

Accepted 2022 February 18. Received 2022 February 17; in original form 2021 April 29

## SUMMARY

Airborne systems collecting transient electromagnetic data are able to gather large amounts of data over large areas in a very short time. These data are most often interpreted through 1-D inversions, due to the availability of robust, fast and efficient codes. However, in areas where the subsurface contains complex structures or large conductivity contrasts, 1-D inversions may introduce artefacts into the models, which may prevent correct interpretation of the results. In these cases, 2-D or 3-D inversion should be used. Here, we present a 2.5-D inversion code using 3-D forward modelling combined with a 2-D model grid. A 2.5-D inversion is useful where the flight lines are spaced far apart, in which case a 3-D inversion would not add value in relation to the added computational cost and complexity. By exploiting the symmetry of the transmitter and receiver system we are able to perform forward calculations on a reduced 3-D mesh using only half the domain transecting the centre of the transmitter and receiver system. The forward responses and sensitivities from the reduced 3-D mesh are projected onto a structured 2-D model grid following the flight direction. The difference in forward calculations is within 1.4 per cent using the reduced mesh compared to a full 3-D solution. The inversion code is tested on a synthetic example constructed with complex geology and high conductivity contrasts and the results are compared to a 1-D inversion. We find that the 2.5-D inversion recovers both the conductivity values and shape of the true model with a significantly higher accuracy than the 1-D inversion. Finally, the results are supported by a field case using airborne TEM data from the island of Mayotte. The inverted flight line consisted of 418 soundings, and the inversion spent an average of 6750 s per iteration, converging in 16 iterations with a peak memory usage of 97 GB, using 18 logical processors. In general, the total time of the 2-D inversions compared to a full 3-D inversion is reduced by a factor of 2.5 while the memory consumption was reduced by a factor of 2, reflecting the half-mesh approach.

**Key words:** Electrical properties; Hydrogeophysics; Controlled source electromagnetics (CSEM); Inverse theory; Numerical modelling.

## 1 INTRODUCTION

The transient electromagnetic method (TEM) has found widespread use in geophysical surveying for a number of purposes such as groundwater investigation (e.g. Fitterman 1987; Auken *et al.* 2009; Kirkegaard *et al.* 2010), mineral exploration (Smith & Koch 2006; Yang & Oldenburg 2012) and onshore hydrocarbon investigations (Wright *et al.* 2002). Given the compact system configuration and the TEM method being non-invasive, it has the potential to cover large geographical areas in a short time-span. For this reason, several airborne systems have been devised (Lane *et al.* 2000; Sørensen & Auken 2004; Witherly *et al.* 2004), all able to gather huge amounts of data in a matter of hours. The acquired data from loop source TEM systems (ground-based and airborne) are most often inverted with 1-D inversion codes (e.g. Farquharson & Oldenburg 1993; Christensen 2002; Scholl *et al.* 2009; Auken *et al.* 2015) due to speed and their ability robustly to invert almost any type of data. With enough spatially distributed data, the 1-D codes can be used for making quasi 2-D or even 3-D inversions where 1-D inversions (models) of the individual soundings share information through spatial constraints (Auken *et al.* 2005; Viezzoli *et al.* 2009). These inversions provide detailed conductivity distributions of the subsurface, which in turn are used for various geological or hydrological interpretations. However, the aforementioned 1-D and the quasi 2-D and 3-D inversions are based on the approximation that the subsurface is locally 1-D, which can cause interpretation problems in areas with significant 2-D and 3-D effects (Goldman *et al.* 1994; Wilson *et al.* 2006; Yogeshwar & Tezkan 2018). 1-D inversion schemes may well minimize the misfit between observations and model responses satisfyingly, but nevertheless provide an erroneous conductivity model. This predominantly happens in areas with large lateral conductivity gradients where the assumptions behind the 1-D inversion break down and artefacts are introduced in the inverted conductivity models (Ley-Cooper *et al.* 2010). Hence, to get a more accurate conductivity model free of these artefacts, a forward and inversion code modelling the data in 2-D or 3-D is needed. Through the years, several codes have been developed for performing inversions of frequency EM (FEM) and time-domain EM (TEM) data in 3-D (e.g. Newman & Commer 2005; Boerner *et al.* 2008; Cox *et al.* 2010; Zhang *et al.* 2021) as well as codes for performing 2-D and 2.5-D inversion of FEM data (e.g. Wilson *et al.* 2006; Key 2012; Li *et al.* 2016; Boesen *et al.* 2018). Different approaches have been proposed for 2-D inversion of airborne TEM data; Wolfgram *et al.* (2003) produced a code using the fast approximate inverse mapping (AIM; Oldenburg & Ellis 1991); however, this method had to rely on multiple components of the magnetic field to reproduce the true conductivity, complicating calculations and field measurements. Guillemoteau *et al.* (2012) devised a fast 2-D inversion scheme using an empirical model describing the 2-D sensitivity for an in-loop configuration, which is of limited use outside of an in-loop configuration.

In this paper, we propose a 2.5-D TEM inversion scheme. We apply the finite-element (FE) time-domain method (FETD) to calculate the full 3-D forward responses and sensitivities on 3-D tetrahedral meshes while mapping the conductivity models on a 2-D grid. We here assume the conductivity along strike (perpendicular to the flight line) to be homogeneous. With this assumption, we exploit the symmetry of the transmitter/receiver system and only calculate the forward solution on one half of the 3-D domain, which allows us to speed up calculations by 2–4 times. The 2.5-D inversion scheme is justified in regional surveys where flight lines are space so far apart that the footprints of neighbouring lines do not overlap, and hence a full 3-D solution is not needed. The benefit of the 2.5-D solution compared to the 3-D solution is a far simpler and numerical efficient inversion scheme. We verify our symmetry approach by comparing the forward and Jacobian solutions for a full 3-D mesh and a reduced half-domain 3-D mesh to see that they are comparable and show that the computation time of the half-domain solution is significantly faster. We move on to invert a synthetic example constructed to exhibit 2-D artefacts in 1-D inversions and show that our 2.5-D code reconstructs the true model without these 2-D artefacts. Finally, we use the code to invert an 11.7 km long real-world survey line from the volcanic island of Mayotte.

## 2 FORWARD MODELLING

### 2.1 Boundary value problem

In our 2.5-D inversion scheme, we compute the full 3-D forward response following Zhang *et al.* (2021), where the response is calculated using the FE method on an unstructured tetrahedral mesh. The governing boundary value equations are presented in the following, while the adjustments made to Zhang *et al.* (2021), which were needed to optimize the scheme for 2.5-D modelling, are outlined in the next paragraph.

We formulate the boundary-value problem using Maxwell's equations of induction, with the electric- and magnetic-field intensity $\mathbf{E} = \mathbf{E}(\mathbf{r}, t)$, $\mathbf{H} = \mathbf{H}(\mathbf{r}, t)$ for $\mathbf{r} \in \Omega$ and $t \in \mathbb{R}$, where $\boldsymbol{r}$ is the spatial coordinate, $t$ is time and $\Omega$ is the domain in which we calculate the solution:

$$\nabla \times \mathbf{E} = -\mu \frac{\partial \mathbf{H}}{\partial \mathrm{t}}, \tag{1}$$

and

$$\nabla \times \mathbf{H} - \frac{\partial \mathbf{D}(\mathbf{r}, t)}{\partial \mathrm{t}} = \mathbf{J}(\mathbf{r}, t). \tag{2}$$

Here, $\mu = \mu_0 = 4\pi \times 10^{-7}$ Vs A$^{-1}$ m$^{-1}$ is the magnetic permeability of free space, $\mathbf{D}$ is the dielectric displacement and $\mathbf{J}$ is the current density. We use the quasi-static approximation (Ward & Hohmann 1988), ignoring displacement currents such that $\frac{\partial \boldsymbol{D}}{\partial t} = 0$, and assume that the medium is linear, isotropic and does not exhibit dispersion. Adding a source current, $\mathbf{j_s} = \mathbf{j_s}(\mathbf{r}, \mathrm{t})$ to eq. (2) and using $\mathbf{J} = \sigma \mathbf{E}$, where $\sigma = \sigma(\mathbf{r})$ is the electric conductivity, we get

$$\nabla \times \mathbf{H} = \sigma \mathbf{E} + \mathbf{j_s}. \tag{3}$$

Finally, we substitute eq. (3) into eq. (1) and rearrange to end up with

$$\nabla \times \nabla \times \mathbf{E} + \mu\sigma \frac{\partial \mathbf{E}}{\partial \mathrm{t}} = -\mu \frac{\partial \mathbf{j_s}}{\partial \mathrm{t}}, \tag{4}$$

which is the first equation in our boundary-value problem, which is valid for $\mathbf{r} \in \Omega$. We impose Dirichlet boundary condition on the boundaries of the domain, $\Gamma$, such that

$$\mathbf{E}(\mathbf{r}) = \mathbf{g}, \mathbf{r} \in \Gamma, \tag{5}$$

where $\mathbf{g}$ is the electromagnetic field on the domain boundary. Eqs (4) and (5) comprise our boundary-value problem for the solution of the forward problem. We use an edge-based FE discretization and thus further state this boundary-value problem in a weak form:

$$\int\int\int_{\Omega} \frac{1}{\mu} (\nabla \times \mathbf{N}) \cdot (\nabla \times \mathbf{E}) + \sigma \mathbf{N} \cdot \frac{\partial \mathbf{E}}{\partial \mathrm{t}} + \mathbf{N} \cdot \frac{\partial \mathbf{j_s}}{\partial \mathrm{t}} \mathrm{d}\Omega = 0. \tag{6}$$

Using the FE method, the electric fields are discretized on each edge of tetrahedral elements and the boundary-value problem converts to a system of linear equations (see Appendix A), which is solved using the PARDISO solver found in the MKL library (Schenk & Gärtner 2004).

### 2.2 Reduced 3-D meshing

The 2.5-D inversion scheme is based on two different types of meshes: a 2-D regular structured model grid, where the model-space conductivity is defined in the nodes, and one 3-D unstructured tetrahedral mesh for calculating the 3-D forward response of each sounding, that is one separate (local) 3-D mesh per sounding (Fig. 1).

The 2.5-D method is primarily devised for airborne or towed ground-based data where the data lines are spaced sufficiently far apart such that it is not meaningful to extract 3-D information due to non-overlapping sensitivities. Compared to a full 3-D solution, we use the principle of symmetry, so we only need to calculate the forward response in one half of the 3-D mesh, which is a clear computation advantage.

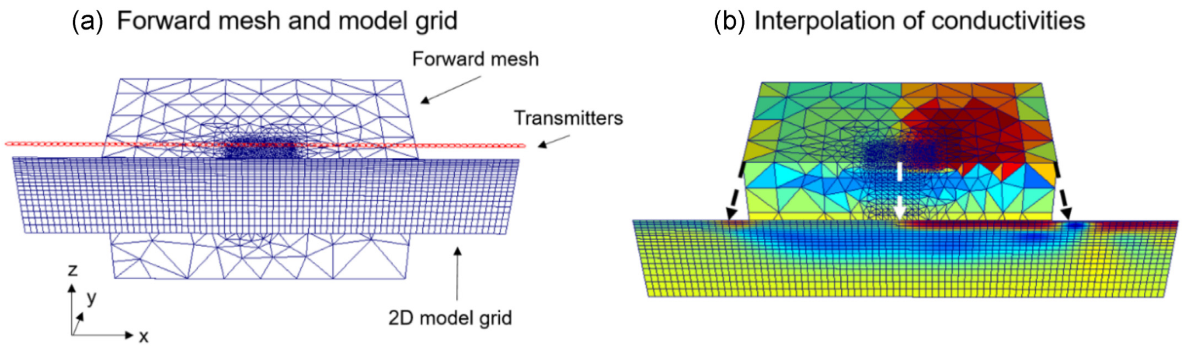


**Figure 1.** (a) The full regular 2-D model grid consisting of 81 horizontal nodes (one for each sounding) located directly beneath the transmitter (red circles). Behind the model grid, one of the halved 3-D forward meshes is shown (the forward mesh of the middle sounding/transmitter. (b) The result of interpolating the conductivities from the nodes of the model grid to the cells of the forward mesh. Note that the model grid has been displaced to show the conductivity structure in the forward mesh.

Letting the $x$-axis be oriented in the flight direction, we divide the full mesh of each sounding half through the $xz$-plane passing through the centre of the transmitter and receiver system, as shown in Fig. 1(a). Assuming that the conductivities are constant from cell to cell along the $y$-axis and due to the symmetry of the system, the magnetic field is symmetric about the $xz$-plane and consequently, $B_y = 0$. Then, according to Faraday's law $E_x = 0$ and $E_z = 0$ are implemented as the boundary condition along the $xz$-symmetry plane, $\Pi$, such that

$$E_x(\mathbf{r}) = 0 \text{ and } E_z(\mathbf{r}) = 0, \quad \mathbf{r} \in \Pi. \tag{7}$$

The conductivity is defined and updated in the nodes of the 2-D model grid. The forward response and the conductivity is transferred between the 2-D model grid and the cells of the 3-D forward mesh through an interpolation function $f$ using inverse distance following the procedure of Christensen *et al.* (2017):

$$\mathbf{p} = f(\hat{\mathbf{p}}) = \mathbf{F}\hat{\mathbf{p}} \tag{8}$$

where $\mathbf{p}$ is a vector containing the model parameter values from the 3-D meshes, $\hat{\mathbf{p}}$ contains the parameter values from the 2-D model grid and $\mathbf{F}$ is a transformation matrix containing the interpolation weights, which only depend on the relative distances. An example of the half-domain (reduced) 3-D forward mesh and 2-D model grid is shown in Fig. 1, which also illustrates the transferred conductivity values from 2-D grid to 3-D mesh. The example illustrates a flight line with 81 soundings (i.e. 81 transmitter and receiver locations). Thus the forward mesh must be shifted 81 times along the model grid, and the interpolation between the forward mesh and the model grid must be repeated each time. Since we use unstructured tetrahedral meshes to compute the forward response, the conductivity profile will change along the $y$-axis despite the 2-D formulation of the model parameters. This is due to the size of the elements becoming larger away from the centre; however, this does not matter as long as the change is not significant within the size of the system footprint.

The 2-D model grid used for inversion is constructed by placing a grid node at each sounding location from the flight line that is inverted. A number of vertical nodes are added according to the number of layers chosen for the inversion, and hence we obtain a regular and structured model grid. The forward meshes are constructed using the open source Delauney-based tetrahedral mesh generator TetGen (Si 2015). We join the information from the sequential forward meshes through the constraints in the model grid and through a common sensitivity matrix.

## 3 SENSITIVITY CALCULATIONS

For the sensitivity computations, we follow the idea of Zhang *et al.* (2021), where the forward calculations and the sensitivity calculations are done on separate meshes. Both the forward and the sensitivity is computed on unstructured tetrahedral meshes, but the separation of the two meshes makes it possible to use a coarser mesh for the sensitivity computation, which speeds up the sensitivity computation significantly without decreasing the forward accuracy (Zhang *et al.* 2021). As for the forward response, a separate (local) mesh is used for each sounding to compute the sensitivity values.

The sensitivity matrix, $\mathbf{J}$, is computed following the adjoint forward modelling method. Assuming the forward modelling matrix equation to be $\mathbf{Ke} = \mathbf{b}$, where $\mathbf{e}$ is the electric field, $\mathbf{b}$ is the source term and $\mathbf{K}$ is the stiffness matrix, then the Jacobian matrix can be obtained by solving the matrix equation of $\mathbf{K}^{\mathrm{T}}\mathbf{V} = \mathbf{L}^{\mathrm{T}}$, where $\mathbf{L}$ is the interpolation vector, so

$$\mathbf{J}^{\mathrm{T}} = \mathbf{G}^{\mathrm{T}}\mathbf{V} = \left(\frac{\partial \mathbf{b}}{\partial \mathbf{m}} - \frac{\partial \mathbf{K}}{\partial \mathbf{m}}\mathbf{e}\right)\left(\mathbf{K}^{-1}\right)^{\mathrm{T}}\mathbf{L}^{\mathrm{T}}. \tag{9}$$

The Jacobian is interpolated from the 3-D mesh unto the 2-D model grid in the same way as the forward response using the definition of the interpolation function in eq. (8), so

$$\mathbf{J}_{\hat{\mathrm{p}}} = \mathbf{J}_{\mathrm{p}}\mathbf{F}^{\mathrm{T}}, \tag{10}$$

where $\mathbf{J}_{\mathrm{p}}$ is the Jacobian in the 3-D mesh and $\mathbf{J}_{\hat{\mathrm{p}}}$ is the Jacobian in the 2-D model grid.

Calculating all the sensitivity values is computationally intensive when there are many time steps, as they are calculated using a backward routine. This means that the sensitivities are calculated for the last time step $t_n$ first, and subsequently for time steps $t_{n-1}, \ t_{n-2} \ldots t_1$. ($n$ is typically between 150 and 250 depending on the time-gates used in the data acquisition). For each time step calculated, all the preceding time steps must be calculated, thus calculating the sensitivities for $t_1$ is much more computationally intensive than calculating sensitivities at time step $t_{n-1}$. Hence, to avoid performing lengthy and unnecessary calculations, we only calculate sensitivities on a subset of the mesh, ideally approximating the size of the system footprint. In practice, we chose the size of the subset mesh by testing different sizes while inverting a synthetic example and looking for the predictive strength for recovering the true model balanced versus number of iterations and iteration time. We found that a smaller mesh leads to faster calculations, but required more iterations to converge, and the resulting model was less accurate.

**Table 1.** Airborne system specifications.

| Segmented loop area | Max current | Ramp-down time | Flight height |
|---|---|---|---|
| 337 $m^2$ | 1 A | 3.75 μs | 50 m |

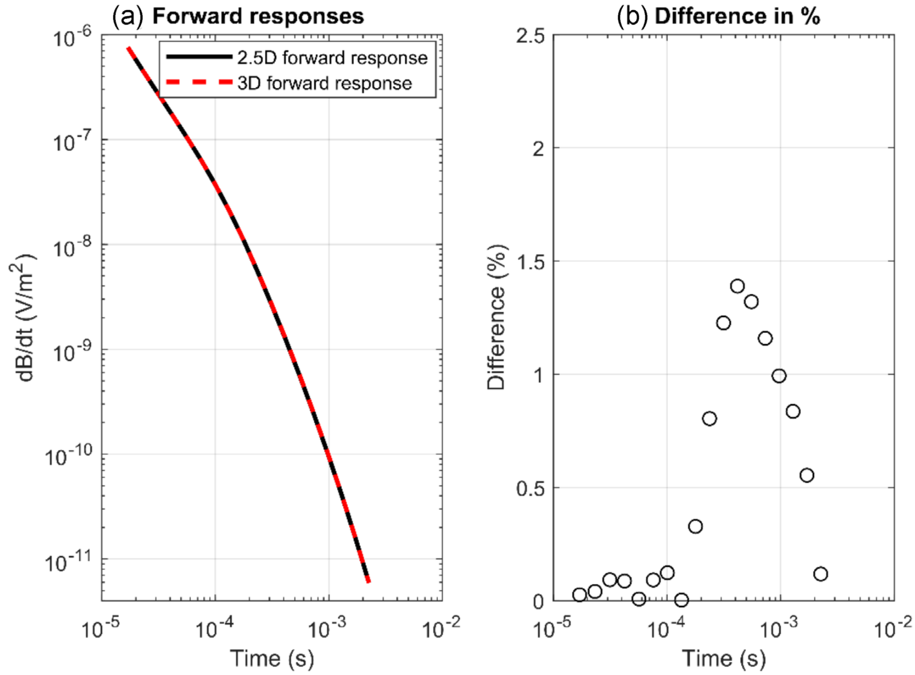


**Figure 2.** (a) 3-D forward response compared to 2.5-D forward response (i.e. the 3-D response on the reduced mesh) calculated on a two-layer model with the upper layer having a resistivity 50 Ω m and a thickness of 50 m, while the lower layer has a resistivity of 300 Ω m. (b) The relative difference at each time gate in percentages.

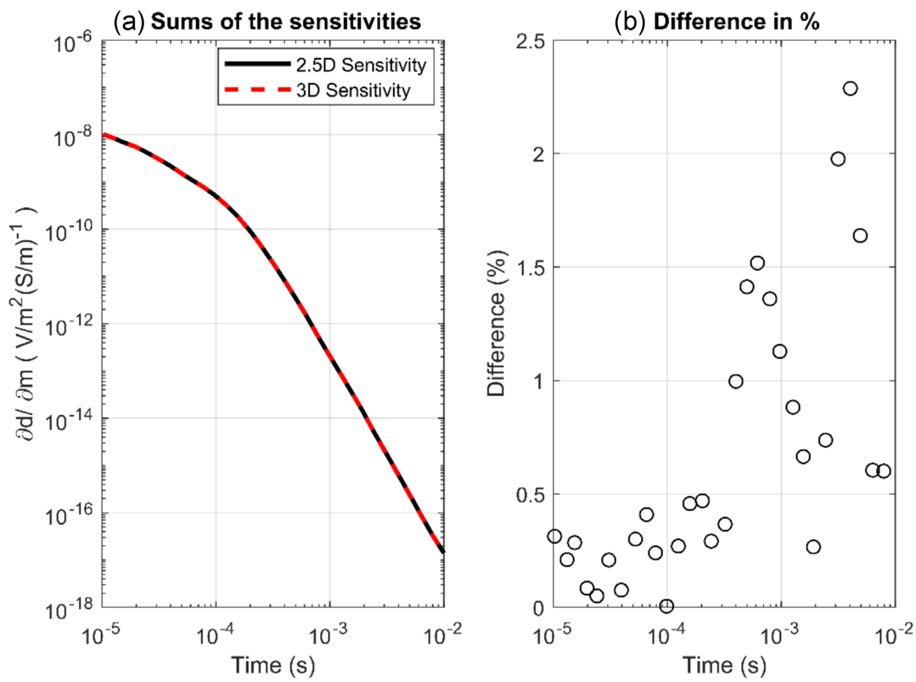


**Figure 3.** (a) The sum of the calculated sensitivities from the model grid using the full 3-D solution and the 2.5-D solution (3-D forward on the reduced mesh). (b) The relative difference in percentage between the summed energy shown in time gate.

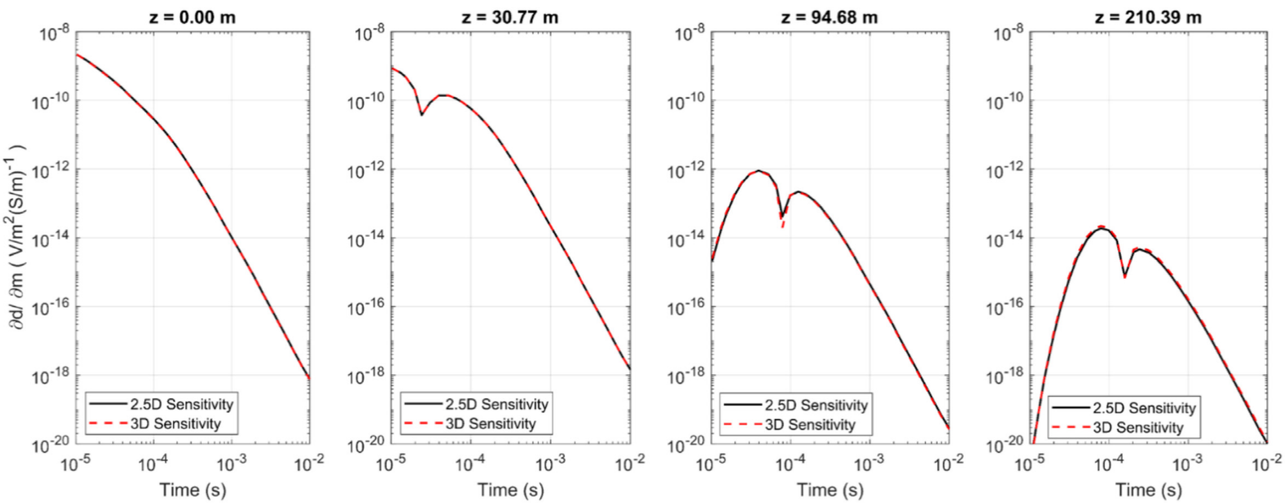


**Figure 4.** The sensitivity calculations for various depths ($z$) for the 3-D and 2.5-D (3-D forward on the reduced mesh) calculations. The results shown here are taken after interpolation from the 3-D sensitivity mesh to the 2-D model grid.

Conversely, using a larger mesh lead to slower calculations, but convergence was reached in fewer iterations and resulted in a more accurate model. Setting the subset mesh to be very large simply increased the calculation time for each iteration, but did not lead to a faster convergence or more accurate model. Thus, at a given size of subset mesh, the accuracy of the resulting model only improves marginally while computation times keep rising. This transition was found to be at a subset mesh size of 400 × 400 × 600 m$^3$ centred on the transmitter location. An airborne system was simulated in testing the optimal size of the subset mesh for the sensitivity calculations, the specifications of the system can be seen in Table 1.

## 4 ITERATIVE INVERSION SCHEME

The inversion uses a Marquardt-damped Gauss–Newton scheme for calculating the parameter update where the objective function is given as follows:

$$Q = \left( \frac{1}{N+M+A} \sum_{i=1}^{N+M+A} \delta \mathbf{d}'^{\mathrm{T}} \mathbf{C}'^{-1} \delta \mathbf{d}' \right)^{\frac{1}{2}} . \tag{11}$$

Here, N, M and A are the numbers of observed data, of prior data and of regularizing constraints, respectively (Auken & Christiansen 2004). $\delta\mathbf{d}'$ and $\mathbf{C}'$ are given by

$$\mathbf{C}' = \begin{bmatrix} \mathbf{C}_{\mathrm{obs}} & & 0 \\ & \mathbf{C}_{\mathrm{prior}} & \\ 0 & & \mathbf{C}_R \end{bmatrix} , \tag{12}$$

and

$$\delta\mathbf{d}' = \begin{bmatrix} \delta\mathbf{d} \\ \delta\mathbf{m} \\ \delta\mathbf{r} \end{bmatrix} = \begin{bmatrix} \mathbf{d} - \mathbf{d}_{\mathrm{obs}} \\ \mathbf{m} - \mathbf{m}_{\mathrm{prior}} \\ \mathbf{Rm} \end{bmatrix} . \tag{13}$$

$\mathbf{C}_{\mathrm{obs}}$, $\mathbf{C}_{\mathrm{prior}}$ and $\mathbf{C}_R$ are the covariances on the observed data, the prior information and the roughness constraints, respectively. $\delta\mathbf{d}$, $\delta\mathbf{m}$ and $\delta\mathbf{r}$ are the differences between the observed data and the forward responses, the current model parameters and the prior model parameters, and the model roughness. The parameter update at iteration $n+1$ is then calculated as

$$\mathbf{m}_{n+1} = \mathbf{m}_n + \left[ \mathbf{G}_n'^{\mathrm{T}} \mathbf{C}'^{-1} \mathbf{G}_n' + \lambda_n \mathbf{I} \right]^{-1} \cdot \left[ \mathbf{G}_n'^{\mathrm{T}} \mathbf{C}'^{-1} \delta\mathbf{d}_n' \right] , \tag{14}$$

where $\mathbf{m}_n$ is the $n$'th model vector, $\mathbf{I}$ is the identity matrix and $\mathbf{G}'$ is given by

$$\mathbf{G}' = \begin{bmatrix} \mathbf{G} \\ \mathbf{P}_{\mathrm{prior}} \\ \mathbf{R} \end{bmatrix} , \tag{15}$$

where $\mathbf{G}$ is the full sensitivity matrix, $\mathbf{P}_{\mathrm{prior}}$ contains the constraints on the prior information and $\mathbf{R}$ is the roughness matrix. $\lambda_n$ is a damping parameter used to stabilize the inversion of the matrix $\mathbf{G}_n'^{\mathrm{T}} \mathbf{C}'^{-1} \mathbf{G}_n'$ in eq. (14) and control the size of the model update (Marquardt 1963; Auken *et al.* 2015). For a thorough explanation of the matrices and vectors we refer the reader to Zhang *et al.* (2021).

## 5 RESULTS

### 5.1 Verification of forward response and sensitivity

We now demonstrate that the forward calculations performed on a reduced (half-domain) 3-D forward mesh produce approximately the same responses as the calculations on the full 3-D forward mesh. The forward response for the full 3-D mesh has previously been verified against a semi-analytical 1-D code (Zhang *et al.* 2021). The forward calculations are made on a two-layered half-space. We furthermore show that the sensitivity calculations for the given sounding are approximately the same. In this comparison, it is ensured that the coinciding parts of the meshes are similar in their discretization, meaning they contain approximately the same amount of edges, points, and elements.

We use a two-layer model with a 50 m thick upper layer that has a resistivity value of 50 Ω m. The lower layer extends indefinitely and has a resistivity value of 300 Ω m. The source and receiver are modelled as an airborne segmented central-loop system, and specifications can be seen in Table 1. The model grid consists of 21 vertically and logarithmically spaced nodes from a depth of 0–300 m. The results of the forward calculations are presented in Fig. 2. The difference between the calculated fields is at a maximum of 1.5 per cent seen at a time of $5^{-4}$ s, suggesting that exploiting the symmetry of the transmitter and receiver system and performing calculations on one half of the 3-D mesh is almost as accurate as calculations on a full 3-D mesh. As the full 3-D and half 3-D mesh are not exactly the same, we compare the sensitivity calculations after

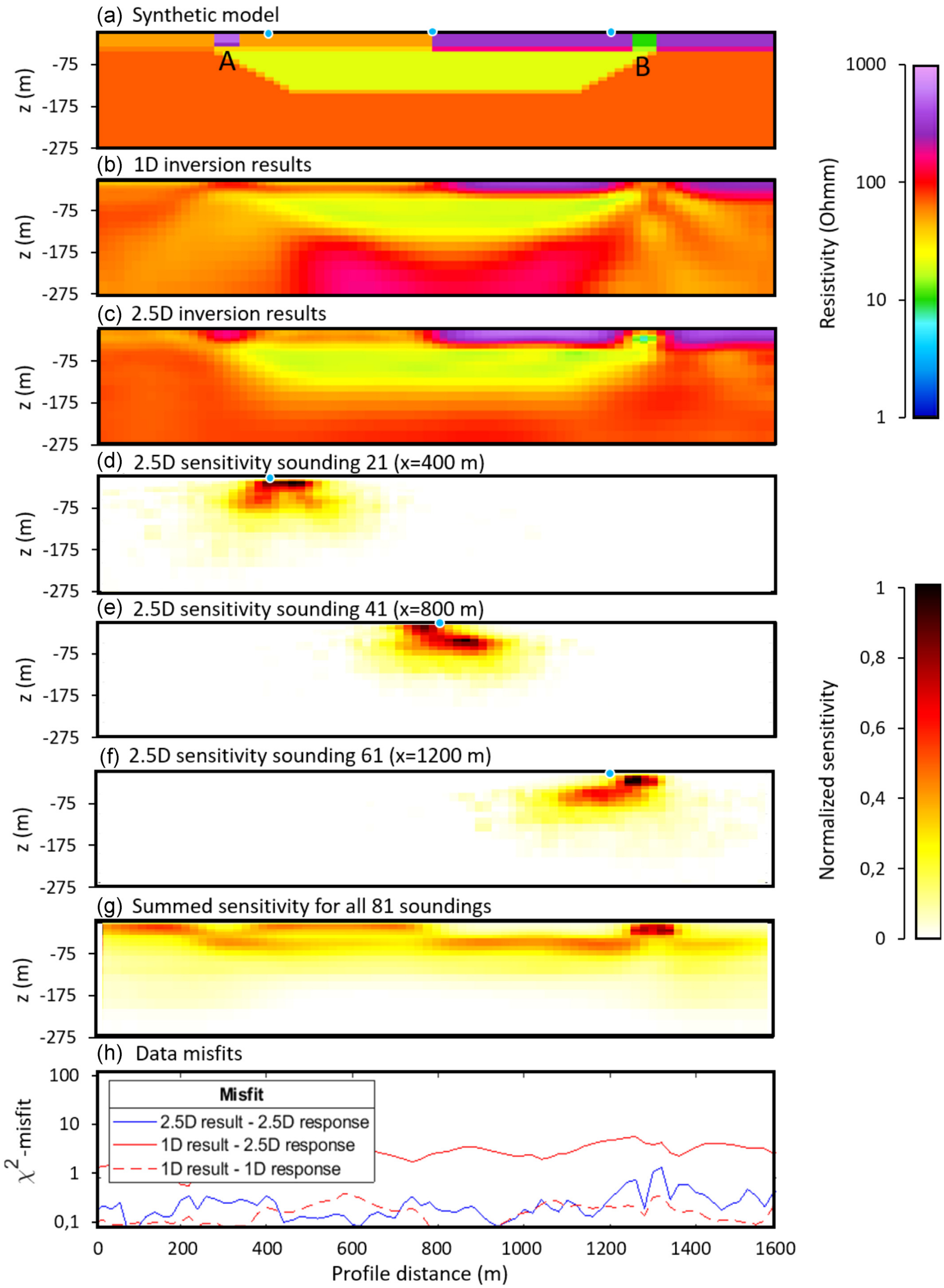


**Figure 5.** Inversions of synthetic data. (a) A visualization of the true model. The model consists of a profile covering 1600 m and a depth of 300 m. It is a valley model with an overburden with different resistivities in the left and right half with channels running through in each side (a and b). The channels pose large conductivity contrasts to the rest of the overburden. (b) The 1-D inversion results. (c) The 2.5-D inversion results. (d–f) The 2.5-D sensitivity for three soundings. The sensitivity (V/m$^2$(S/m)$^{-1}$) has been summed for all time gates for each sounding and normalized by the maximum sensitivity to get a relative distribution between 0 and 1. The blue dots indicate the location of the centre of the transmitter loop on both the sensitivity plots and the true model. (g) The summed sensitivity of all 81 soundings combined. (h) The data misfit for each sounding plotted along the profile. The misfit is shown as the misfit between the 2.5-D forward data of the synthetic model and the 2.5-D response of the 2.5-D inversion result (blue curve), the 2.5-D response of the 1-D inversion results (red curve), and the 1-D response of the 1-D inversion result (red dashed curve).

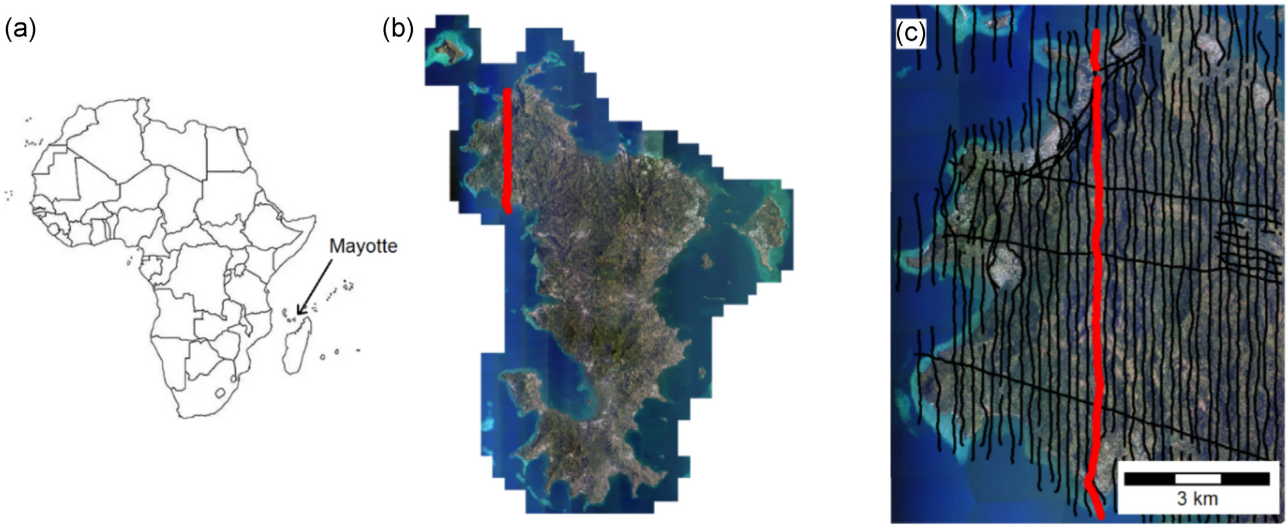


**Figure 6.** (a) The island of Mayotte situated between Africa and Madagascar. (b) The island of Mayotte with the location of the 11.7 km flight line applied in this study (red line). (c) Close-up of the 11.7 km flight line (red line) running from the sea through urban areas and above a mountain ridge. The flight lines not used in this study are shown in black.

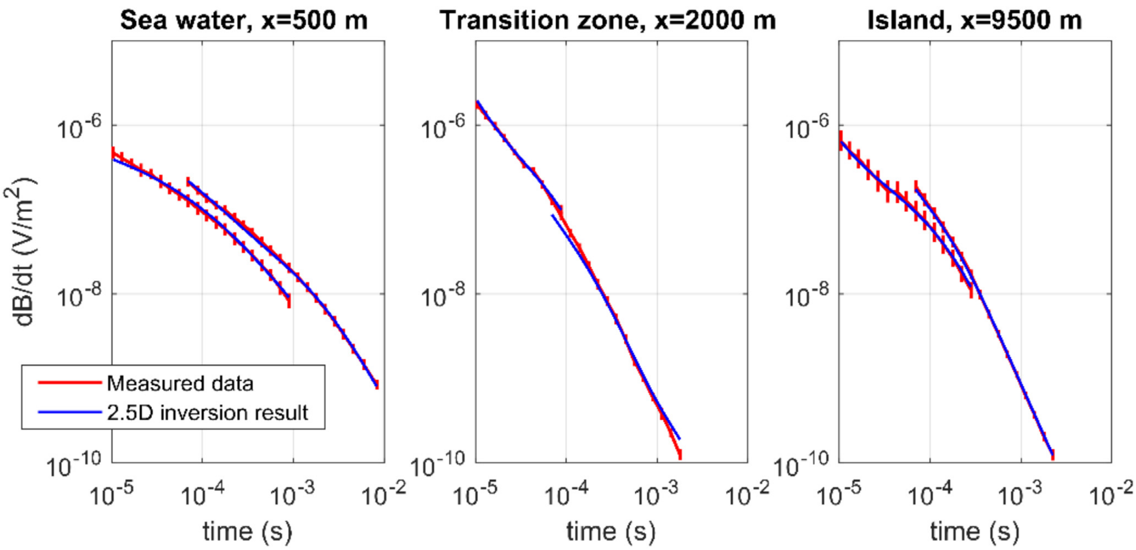


**Figure 7.** The data fit shown for the inversion of field data from Mayotte Island for three soundings along the resistivity section shown in Fig. 8(a). The red curves are the measured data with two standard deviation error bars, and the blue curves are the inversion results. Each sounding consists of a low-moment and a high-moment measurement. The x-location refers to the x-coordinate in Fig. 8(a).

the transformation from the three-dimensional meshes to the model grid. This allows us to do a spatial comparison that is almost 1-to-1, and looking at the summed sensitivities shown in Figs 3(a) and (b), the maximum difference between them is seen to be approximately 2.3 per cent in the time-range of our soundings. In Fig. 3, we interpolate the sensitivity to the same time channel. However, the time steps used in the reduced 3-D and the full 3-D forward modelling are different from each other. This increases the reliability of the verification. In Fig. 4, a comparison of the sensitivity calculations is shown for four depths directly underneath the transmitter. The largest difference in these is seen at a depth of 210 m where the sensitivity in the full 3-D mesh is slightly higher. However, we do not consider this to be significant for our inversion.

The time spent on calculations for the forward calculations was 88 s for the half-domain and 217 s for the full-domain, while calculating the sensitivity was done in 361 s for the half-domain and 915 s for the full-domain, suggesting a speed-up factor of 2.5 for a single sounding using one CPU core. The peak memory consumption was 717 MB for the half-domain case and 1347 MB for the full domain and occurred during the computation of the sensitivities.

### 5.2 Inversion of synthetic data

Through a synthetic study we here demonstrate that our 2.5-D code accurately reconstructs a conductivity model exhibiting pronounced 2-D effects when inverted by a 1-D code. It is well known that 1-D inversions suffer from 2-D or 3-D effects when the subsurface cannot be approximated as one-dimensional and the conductivity gradient is large (Goldman *et al.* 1994; Wilson *et al.* 2006; Yogeshwar & Tezkan 2018), which is why we constructed a model with a complex structure and high conductivity contrasts. The model we use for this demonstration resembles a valley with a variable

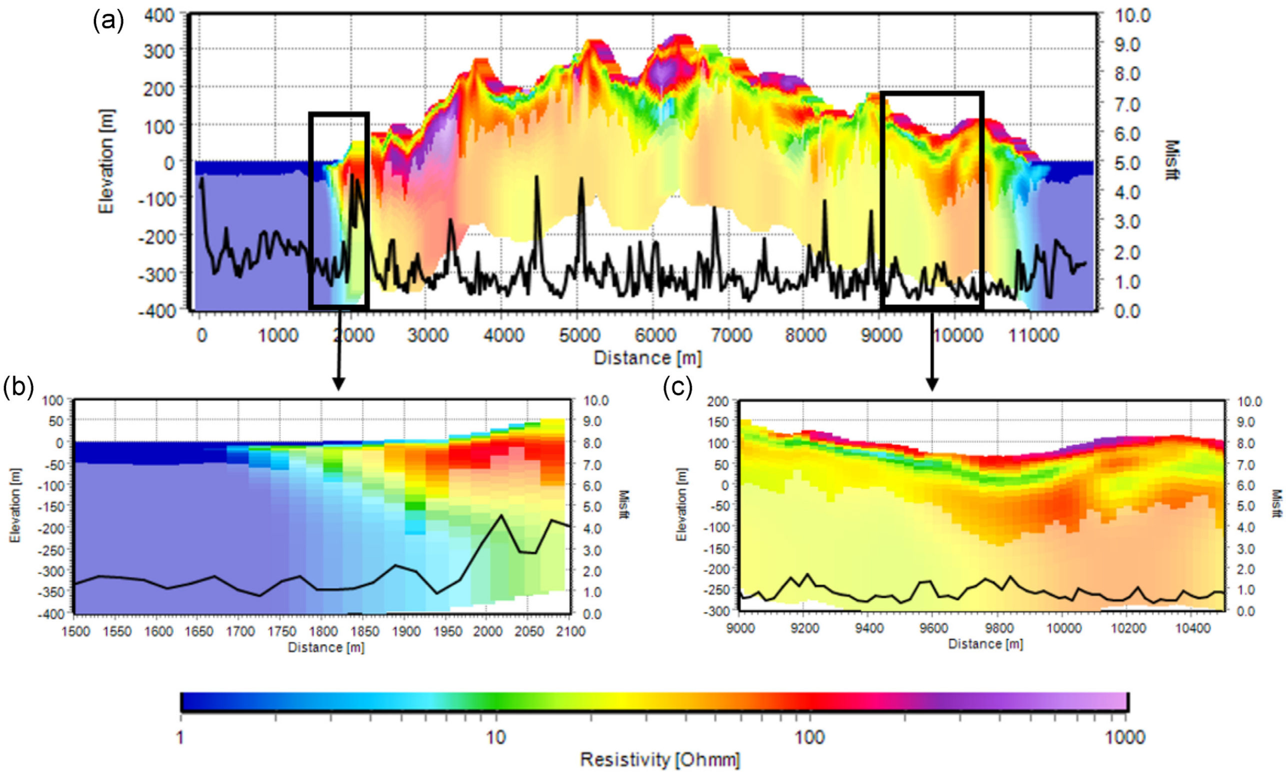


**Figure 8.** The 2.5-D inversion results of data from the line shown on the map in Fig. 6, seen north to south (left to right). The black line is the data misfit, and the depth of investigation (DOI) is shown as the white shadow. (a) The resistivity profile of the entire flight line. (b) A close-up of sea-land transition. (c) A close-up close to a volcanic crater.

overburden as seen in Fig. 5(a). In the overburden, we have put two channels (A and B) with large conductivity contrasts placed just above the sloping sides of the valley, a setup that is prone to introducing artefacts in a 1-D inversion. The valley itself has sloping sides, a flat valley floor, and a moderate conductivity contrast relative to the background.

The simulated survey consists of the aforementioned airborne system and specifications can be seen in Table 1. The length of the section is 1600 m with soundings every 20 m, for a total of 81 soundings. Both inversions (1-D and 2.5-D) are carried out using the same lateral and vertical constraints in the model parameter grids in an LCI scheme (Auken *et al.* 2008), allowing the same variation in the models. The final data residual for the 1-D inversion is 0.24 while it is 0.44 for the 2.5-D inversion considering 3 per cent standard deviation on the data. The residuals are calculated using eq. (11), but only including the data parts of the vectors and matrices. The inversion results are seen in Figs 5(b) and (c).

It is seen that the 1-D inversion roughly recovers the true model. The valley is present, the overburdens are present as well, as are the features in the overburden, albeit smeared. However, the shape of the valley infill is more rounded than that of the true model, and the resistivity of the channels A and B, are not accurate. Pant-leg effects can be seen radiating out and downwards originating from the sides of the valley between 250 and 400 m. These effects are also seen on the opposite side manifested as two distinct rays originating just below channel B. Finally, it is seen that the resistivity below the valley between 600 and 1100 m is overestimated in comparison to the true model.

Looking at the 2.5-D inversion (Fig. 5c), it is seen that it recovers the true model much better than the 1-D inversion. The background resistivity is well recovered in most of the model with slight variations seen just below the high resistive overburden at 1500 m. However, the resistivity below the valley floor is not overestimated as was seen in the 1-D inversion. The shape of the valley infill matches the true model much better than the 1-D inversion, and resistivity in the overburden is also better determined. Notably, both channels (A and B) are much better recovered. We also see notable lack of pant-leg effects along the sloping edges on both sides of the valley.

Figs 5(d)–(f) show the 2.5-D sensitivities computed from the final 2.5-D inversion result for three different soundings along the profile. The sensitivities have been summed in each mesh node for the 18 time gates of the TEM data and then normalized by the maximum sensitivity value to give a relative distribution between 0 end 1. The blue dot on the figure frame indicates the location of the centre of the transmitter loop for the given sounding. The sensitivity distributions become asymmetric below the transmitter due to the asymmetry in the resistivity of the structures. This is most clearly visible in Fig. 5(f) where the conductive feature shifts the sensitivity away from the sounding centre point. Fig. 5(h) shows the summed sensitivity profile for all 81 soundings. We see a relative high sensitivity in the conductive structures, where the current density is high, and low sensitivity in the restive structures. For instance, in Fig. 5(h), the resistive overburden on the right side of the synthetic model ($x = 800$–$1600$ m in Fig. 5a), shows a low sensitivity compared to the conductive channel B. We also note that the sensitivity is locally decreased below channel B because the current stays in the conductive channel material.

Fig. 5(h) shows the data misfit for the 1-D and the 2.5-D inversions. The blue curve is the $\chi^2$-misfit between the 2.5-D forward responses (3-D response on the reduced mesh) of the synthetic model and the final 2.5-D inversion results. The misfit is below 1 (meaning that the response fits the data within the 3 per cent error bars), except below channel B, where the conductivity contrasts are largest. The solid red curve in Fig. 5(h) is the $\chi^2$-misfit between the synthetic data and the 2.5-D forward response (3-D response on the reduced mesh) of the final model in the 1-D inversion results. The dashed red curve in Fig. 5(h) is the $\chi^2$-misfit between the synthetic data and the 1-D forward response of the final model in the 1-D inversion results. The 1-D misfit is below the misfit reached with the 2.5-D inversion, which shows how the 1-D misfit can be misleading if 2-D or 3-D effects are present in the data.

Overall, the 2.5-D inversion code is a substantial improvement in the reconstruction of the true model compared to the 1-D inversion. The 2.5-D inversion was started from a homogeneous model and converged after 7 iterations with an L2 norm of the difference of 0.55. Each iteration took an average of 20 min (total inversion time approximately 2.5 hr on 25 CPUs) and the peak of memory consumption was about 30 GB of memory.

### 5.3 Inversion of field data

To demonstrate the applicability of the code for inversion of field data inversions we perform an inversion on a single flight line from a TEM data set from the island of Mayotte shown in Fig. 6. The data were acquired using a SkyTEM system (Sørensen & Auken 2004; Sørensen *et al.* 2004) in 2009 as part of a geological mapping project carried out by Aarhus University in collaboration with the French Geological Survey (BRGM). The island of Mayotte is part of the Comoro Islands located in the Mozambique Channel at the southern part of the African continent. It is a volcanic island and the subsurface is primarily made up of volcanic rocks, containing several basalt aquifers (Lachassagne *et al.* 2014). The main formations are Miocene and Pliocene basaltic and phonolitic lavas as well as pyroclastic deposits with different degrees of weathering affecting their hydrological properties (Vittecoq *et al.* 2014). Approximately 3000 km of data were collected covering the entire island with 200 m spacing between the flight lines.

The inverted flight line is 11.7 km with a total of 418 soundings and runs from coast to coast on the northeastern part of the island as seen on Figs 6(b) and (c). Each sounding consists of a low and a high moment measurement (Sørensen & Auken 2004). Examples of the low moment and high moment data measurements are shown in Fig. 7 for three different locations on the flight line. The standard deviation computed for the stacked data is used as the error model in the inversion, which is also shown in Fig. 7.

Smoothness constraints of 0.3 and 1 were applied in the inversion (eqs 13 and 14) in the horizontal and the vertical direction, respectively, between the 2-D model grid nodes. The inversion was started from a homogeneous half-space and converged after 16 iterations with a data residual of 1.2. Each iteration took an average of 6750 s (total inversion time of 30 hr) and was consuming a maximum of 97 GB of RAM. The results of the 2.5-D inversion are shown in Fig. 8 with the misfit of each sounding shown as a black line plotted on top of the profile and the depth of investigation (DOI) shown as a white shadow.

Crossing the coastlines, the flight line (Fig. 6) makes an abrupt transition from the conductive salt-water (~1 Ωm) to a highly resistive geology (30–1000 Ωm), which usually triggers strong 2-D or 3-D effects in a 1-D inversion. In the results of our 2.5-D inversion, Fig 8(a), none of these effects are observed. A detailed view of the northernmost sea-land transition is shown in Fig. 8(b). It is seen that while the data residual increases close to the coast (from a misfit of ~2 to 4), the model shows no apparent 2-D or 3-D effects and looks like a reasonable geological model with highly resistive basaltic materials of different ages and degrees of weathering. The data fit is shown in Fig. 7 for examples with the saltwater, the sea-land transition, and the inland. An inland view of the profile is shown in Fig. 8(c). Here we are close to a volcanic crater, and we see that the top 20–30 m are highly resistive (200–1000 Ωm) overlaying a thin 20–30 m discontinued conductive layer (5–10 Ωm) again overlaying the base of intermedia resistivity (30–100 Ωm).

The resistive top layer is interpreted as slightly weathered Plio-Pleistocene lavas and the conductive layer as a volcanoclastic formation, which is consistent with the resistivities previously described in the literature (Schamper *et al.* 2013; Vittecoq *et al.* 2014). The base below the two layers is interpreted as Miocene weathered lavas.

## 6 CONCLUSION

In this paper, we have presented a novel 2.5-D transient electromagnetic inversion scheme combining a regular structured 2-D model-parameter grid with 3-D tetrahedral meshes on which we calculate both the 3-D forward responses and sensitivities. We have shown that we are able to exploit the symmetry of a transmitter and receiver system and calculate the forward responses on a reduced half-domain mesh, while obtaining results within 1.4 per cent of those from a full-domain mesh. For the sensitivity calculations we showed that the maximum difference between them was 5 per cent, which is acceptable considering that the calculated time steps were not identical. We reported a speed-up of a factor of 2.5 for the half-mesh calculations.

A synthetic example shows that our 2-D code gave significant improvements in the recovery of a valley model prone to exhibit 2-D effects in 1-D inversions. Both the recovered conductivity values and the shape of the valley itself were of a higher accuracy in the 2.5-D inversion compared to a 1-D inversion.

Finally, we showed that the code is viable for inverting long data-lines from a real-world survey in terms of memory and computational time. We did this by inverting a profile from an airborne TEM survey carried out on the island of Mayotte. The survey line consisted of 418 soundings and was geologically complex. The inversion converged in 16 iterations after approximately 30 hr with a peak memory consumption of 97 GB.

## ACKNOWLEDGMENTS

This project was funded by the EU Horizon 2020 project Smart Exploration grant agreement No. 775971, Villum Fonden grant No. 37172 to L.M. Madsen, and the Aarhus University Centre for Water Technology (WATEC).

## DATA AVAILABILITY

Data can be made available by contacting the corresponding author. The 2.5-D TEM inversion code has been implemented in the existing inversion software AarhusInv (hgg.au.dk).

## REFERENCES

Auken, E. & Christiansen, A.V., 2004. Layered and laterally constrained 2D inversion of resistivity data, *Geophysics,* **69,** 752–761.

Auken, E., Christiansen, A.V., Jacobsen, L. & Sørensen, K.I., 2005. Laterally constrained 1D-inversion of 3D TEM data. Proceedings of the Symposium on the Application of Geophyics to Engineering and Environmental Problems, SAGEEP; Bind 1, SAGEEP 2005: Geophysical Solutions for Today's Challenges (s. 533-537).

Auken, E., Christiansen, A.V., Jacobsen, L. & Sørensen, K.I., 2008. A resolution study of buried valleys using laterally constrained inversion of TEM data, *J. appl. Geophys.,* **65,** 10–20.

Auken, E., Christiansen, A.V., Viezzoli, A., Fitzpatrick, A., Cahill, K., Munday, T. & Berens, V., 2009. Investigation on the groundwater resources of the South Eyre Peninsula, South Australia, determined from laterally constrained inversion of tempest data, ASEG Extended Abstracts 2009, p. 1–5, https://doi.org/10.1071/ASEG2009ab121.

Auken, E. *et al.*, 2015. An overview of a highly versatile forward and stable inverse algorithm for airborne, ground-based and borehole electromagnetic and electric data, *Explor. Geophys.,* **2015,** 223–235.

Boerner, R.U., Ernst, O.G. & Spitzer, K., 2008. Fast 3-D simulation of transient electromagnetic fields by model reduction in the frequency domain using Krylov subspace projection, *Geophys. J. Int.,* **173,** 766–780.

Boesen, T., Auken, E., Christiansen, A.V., Fiandaca, G., Kirkegaard, C., Pfaffhuber, A.A. & Vöge, M., 2018. An efficient 2D inversion scheme for airborne frequency-domain data, *Geophysics,* **83,** 13, doi:10.1190/geo2017-0280.1.

Christensen, N.B., 2002. A generic 1-D imaging method for transient electromagnetic data, *Geophysics,* **67,** 438–447.

Christensen, N.K., Ferre, T., Fiandaca, G. & Christensen, S., 2017. Voxel inversion of airborne electromagnetic data for improved groundwater model construction and prediction accuracy, *Hydrol. Earth Syst. Sci.,* **21,** 1321–1337.

Cox, L.H., Wilson, G.A. & Zhdanov, M.S., 2010. 3D inversion of airborne electromagnetic data using a moving footprint, *Explor. Geophys.,* **41,** 250–259.

Farquharson, C.G. & Oldenburg, D.W., 1993. Inversion of time-domain electromagnetic data for a horizontally layered Earth, *Geophys. J. Int.,* **114,** 433–442.

Fitterman, D.V., 1987. Examples of transient sounding for ground-water exploration in sedimentary aquifers, *Ground Water,* **25,** 684–693.

Goldman, M., Tabarovsky, L. & Rabinovich, M., 1994. On the influence of 3-D structures in the interpretation of transient electromagnetic sounding data, *Geophysics,* **59,** 889–901.

Guillemoteau, J., Sailhac, P. & Behaegel, M., 2012. Fast approximate 2D inversion of airborne TEM data: born approximation and empirical approach, *Geophysics,* **77,** WB89–WB97.

Jin, J., 2014. *The Finite Element Method in Electromagnetics,* 3rd edn, Wiley-IEEE Press.

Key, K., 2012. Marine EM inversion using unstructured grids: a 2D parallel adaptive finite element algorithm, in *SEG Technical Program Expanded Abstracts 2012,* pp. 1–5.

Kirkegaard, C., Auken, E., Sonnenborg, T.O. & Jørgensen, F., 2010. Airborne TEM investigations of salinity distribution in coastal aquifers: the Ringkoebing lagoon case, in *AGU Fall Meeting,* San Francisco, USA.

Lachassagne, P., Aunay, B., Frissant, N., Guilbert, M. & Malard, A., 2014. High-resolution conceptual hydrogeological model of complex basaltic volcanic islands: a Mayotte, Comoros, case study, *Terra Nova,* **26,** 307–321.

Lane, R., Green, A.G., Golding, C., Owers, M., Pik, P., Plunkett, C., Sattel, D. & Thorn, B., 2000. An example of 3D conductivity mapping using the TEMPEST airborne electromagnetic system, *Explor. Geophys.,* **31,** 162–172.

Ley-Cooper, A.Y., Macnae, J. & Viezzoli, A., 2010. Breaks in lithology: interpretation problems when handling 2D structures with a 1D approximation, *Geophysics,* **75,** 179–188.

Li, W.-B., Zeng, Z.-F., Li, J., Wang, K. & Xia, Z., 2016. 2.5D forward modeling and inversion of frequency-domain airborne electromagnetic data, *Appl. Geophys.,* **13,** 37–47.

Marquardt, D., 1963. An algorithm for least squares estimation of nonlinear parameters, *SIAM J. Appl. Math.,* **11,** 431–441.

Newman, G. & Commer, M., 2005. New advances in three dimensional transient electromagnetic inversion, *Geophys. J. Int.,* **160,** 5–32.

Oldenburg, D.W. & Ellis, R.G., 1991. Inversion of geophysical data using an approximate inverse mapping, *Geophys. J. Int.,* **105,** 325–353.

Ren, X., Yin, C., Macnae, J., Liu, Y. & Zhang, B., 2018. 3D time-domain airborne electromagnetic inversion based on secondary field finite-volume method, *Geophysics,* **83,** E219–E228.

Schamper, C. *et al.*, 2013. 7. Airborne transient EM methods and their applications for coastal groundwater investigations, in *Groundwater in the Coastal Zones of Asia-Pacific,* pp. 121–153, ed. Wetzelhuetter, C., Springer.

Schenk, O. & Gärtner, K., 2004. Solving unsymmetric sparse systems of linear equations with PARDISO, *Future Gener. Comput. Syst.,* **20,** 475–487.

Scholl, C., Helwig, S.L., Tezkan, B., Goldman, M. & Kafri, U., 2009. 1-D multimodel joint inversion of TEM-data over multidimensional structures, *Geophys. J. Int.,* **176,** 81–94.

Si, H., 2015. TetGen, a Delaunay-based quality tetrahedral mesh generator, *ACM Trans. Math. Softw.,* **41,** 1–36

Smith, R.S. & Koch, R., 2006. Airborne EM measurements over the Shea Creek uranium prospect, Saskatchewan, Canada, in *SEG Technical Program Expanded Abstracts,* pp. 1263–1267.

Sørensen, K.I. & Auken, E., 2004. SkyTEM—a new high-resolution helicopter transient electromagnetic system, *Explor. Geophys.,* **35,** 191–199.

Sørensen, K.I., Sørensen, B., Christiansen, A.V. & Auken, E., 2004. *Interpretation of a Hydrogeophysical Survey—Data from the Highresolution SkyTEM SystemEAGE-NS,* EAGE-NS.

Viezzoli, A., Auken, E. & Munday, T., 2009. Spatially constrained inversion for quasi 3D modelling of airborne electromagnetic data—an application for environmental assessment in the Lower Murray Region of South Australia, *Explor. Geophys.,* **40,** 173–183.

Vittecoq, B., Deparis, J., Violette, S., Jaouen, T. & Lacquement, F., 2014. Influence of successive phases of volcanic construction and erosion on Mayotte Island's hydrogeological functioning as determined from a helicopter-borne resistivity survey correlated with borehole geological and permeability data, *J. Hydrol.,* **509,** 519–538.

Ward, S.H. & Hohmann, G.W., 1988. 4 Electromagnetic theory for geophysical applications, *in Electromagnetic Methods in Applied Geophysics,* pp. 131–311, ed. Nabighian, M.N., Society of Exploration Geophysicists (SEG).

Wilson, G.A., Raiche, A. & Sugeng, F., 2006. 2.5D inversion of airborne electromagnetic data, *Explor. Geophys.,* **37,** 363–371.

Witherly, K.E., Irvine, R.J. & Morrison, E., 2004. The Geotech VTEM time domain helicopter EM system, in *ASEG Extended Abstracts,* pp. 1–4.

Wolfgram, P., Sattel, D. & Christensen, N.B., 2003. Approximate 2D inversion of AEM data, *Explor. Geophys.,* **34,** 29–33.

Wright, D., Ziolkowski, A. & Hobbs, B., 2002. hydrocarbon detection and monitoring with a multi-component transient electromagnetic (MTEM) survey, *Leading Edge,* **21,** 809–944.

Yang, D. & Oldenburg, D.W., 2012. Three-dimensional inversion of airborne time-domain electromagnetic data with applications to a porphyry deposit, *Geophys.,* **77,** B23–B34.

Yogeshwar, P. & Tezkan, B., 2018. Analysing two-dimensional effects in central loop transient electromagnetic sounding data using a semi-synthetic tipper approach, *Geophys. Prospect.,* **66,** 444–456

Zhang, B., Engebretsen, K.W., Fiandaca, G., Cai, H. & Auken, E., 2021. 3D inversion of time-domain electromagnetic data using finite elements and a triple mesh formulation, *Geophys.,* **86,** 1–43.

## APPENDIX A: FINITE-ELEMENT SOLUTION

In the edge-based FE approach (Jin 2014), the electric fields are discretized on the edges of each element in the mesh. Hence, the electric field for each element is calculated as a weighted sum of the electric fields contained in the edges,

$$\mathbf{E}(\mathbf{r}) \approx \mathbf{E}'(\mathbf{r}) = \sum_{i=1}^{n} \mathbf{N}_i(\mathbf{r})\,\mathbf{E}_i, \tag{A1}$$

$n$ being the number of edges on the element, $\mathbf{N}_i$ and $\mathbf{E}_i$ being the interpolation function and electric field for the $i$th edge of the element. $\mathbf{E}$ and $\mathbf{E}'$ are the true and approximate electric fields for a given element. The equation we solve for each individual element $\kappa$ can be obtained by substituting eq. (A1) into eq. (6) and integrating. We then get the following equation:

$$\mathbf{M}^{\kappa}\frac{\partial \mathbf{E}'}{\partial \mathrm{t}} + \mathbf{S}^{\kappa}\mathbf{E}'^{\kappa} = \mathbf{J}^{\kappa}, \tag{A2}$$

where

$$\mathbf{M}^{\kappa} = \int\int\int_{\Omega_\kappa} \mathbf{N}^{\kappa} \cdot \sigma^{\kappa}\mathbf{N}^{\kappa}\,\mathrm{d}V^{\kappa} \tag{A3}$$

$$\mathbf{S}^{\kappa} = \int\int\int_{\Omega_\kappa} \frac{1}{\mu}(\nabla \times \mathbf{N}^{\kappa}) \cdot (\nabla \times \mathbf{N}^{\kappa})\,\mathrm{d}V^{\kappa} \tag{A4}$$

and

$$\mathbf{J}^{\kappa} = \int\int\int_{\Omega} \mathbf{N}^{\kappa} \cdot \frac{\partial \mathbf{j}^{e}}{\partial t}\mathrm{d}V^{\kappa}. \tag{A5}$$

We discretize the derivative $\partial\mathbf{E}/\partial t$ using a second-order Euler approximation such that

$$\frac{\partial \mathbf{E}(t)}{\partial t} = \frac{3\mathbf{E}(t) - 4\mathbf{E}(\mathrm{t} - \Delta t) + \mathbf{E}(t - 2\Delta t)}{2\Delta t}. \tag{A6}$$

where $\Delta t$ is the time step following a discretization of time. By gathering all the equations for each element into a matrix, we finally obtain the following linear system of equations:

$$(3\mathbf{M} + 2\Delta t\mathbf{S})\,\mathbf{E}'^{(i+2)} = \mathbf{M}\left(4\mathbf{E}'^{(i+1)} - \mathbf{E}'^{i}\right) - 2\Delta t\mathbf{J}^{i+2}. \tag{A7}$$

We have one such system of equations for each time step in our solution. The time stepping used here follows the adaptive procedure described in Zhang *et al.* (2021) with the first calculation at 1 ns. Eq. (A7) is solved using the PARDISO solver found in the MKL library (Schenk & Gärtner 2004). We follow the interpolation methods described in Ren *et al.* (2018) to obtain a solution at any point in the domain not located on an edge and at any time, which is needed to retrieve the solution for an arbitrarily located receiver.